

**Journal of Alloys and Compounds 638 (2015) 141-147.**

**DOI: 10.1016/j.jallcom.2015.03.082**

<http://dx.doi.org/10.1016/j.jallcom.2015.03.082>

**Fine-grained BaTiO<sub>3</sub>–MgFe<sub>2</sub>O<sub>4</sub> composites prepared by a Pechini-like process**

Roberto Köferstein<sup>1)\*</sup>, Till Walther<sup>1)</sup>, Dietrich Hesse<sup>2)</sup> and Stefan G. Ebbinghaus<sup>1)</sup>

<sup>1)</sup> *Institute of Chemistry, Martin-Luther-University Halle-Wittenberg,  
Kurt-Mothes-Strasse 2, 06120 Halle, Germany.*

<sup>2)</sup> *Max Planck Institute of Microstructure Physics, Weinberg 2, 06120 Halle, Germany.*

*Dedicated to Professor Christian Robl on the occasion of his 60th birthday.*

\* Corresponding author. Tel.: +49-345-5525630; Fax: +49-345-5527028.  
*E-mail address:* roberto.koefenstein@chemie.uni-halle.de

**Abstract.** The synthesis of BaTiO<sub>3</sub>–MgFe<sub>2</sub>O<sub>4</sub> composite powders by a Pechini-like one-pot process and resulting ceramic bodies is described herein. Phase formation during the decomposition of homogenous (Ba,Ti,Fe,Mg)-gels was monitored up to 1200 °C. Composite powders consisting of BaTiO<sub>3</sub> and MgFe<sub>2</sub>O<sub>4</sub> were obtained after decomposition at 700 °C for 1 h resulting in crystallite sizes of about 10 nm. The shrinkage and sintering behaviour of compacted powders were examined. Sintering at ≥ 1200 °C leads to the formation of hexagonal BaTiO<sub>3</sub> only for composites with a MgFe<sub>2</sub>O<sub>4</sub> content of ≥ 30 wt.%. SEM images of

ceramic bodies reveal that the  $\text{MgFe}_2\text{O}_4$  particles are surrounded by  $\text{BaTiO}_3$  crystallites. Magnetic measurements of both powders and corresponding ceramic bodies show ferrimagnetic behaviour with low coercivities. At high-field and low temperatures an additional small paramagnetic contribution was observed which increases with decreasing  $\text{MgFe}_2\text{O}_4$  content and should be considered by the calculation of the saturation magnetization. Finally, the frequency dependent variation of the relative permittivities of the composites was investigated.

Keywords: *sol-gel synthesis ; X-ray diffraction; magnetic measurements ; dielectric response; sintering; composite; ferrite; barium titanate*

## **1. Introduction**

Multiferroic composite materials are of interest because of their potential applications in advanced technologies e.g. sensors, memories and actuators [1,2,3]. Composites consisting of both ferro/-ferrimagnetic and ferroelectric phases can exhibit a magneto-electrical (ME) coupling effect [4]. In such composites a magnetic field changes the electrical polarisation and an external electric field influences the magnetization. The coupling between the two ferroic properties is influenced by the oxide interfaces. Multiferroic composites consisting of  $\text{BaTiO}_3$  as piezoelectric phase and ferrite spinels as magnetostrictive part (e.g.  $\text{CoFe}_2\text{O}_4$ ) have intensively been investigated [5,6,7]. To produce  $\text{BaTiO}_3\text{--}M\text{Fe}_2\text{O}_4$  (with  $M$  being a divalent metal cation) composites various synthesis routes have been reported, e.g. mixed-oxide-, sol-gel- and hydrothermal routes [8,9,10,11]. Reactions between the  $\text{BaTiO}_3$  and  $M\text{Fe}_2\text{O}_4$  phase often lead to the formation of  $\text{BaFe}_{12}\text{O}_{19}$  [12] and hexagonal  $\text{BaTiO}_3$  [13]. Up to now,  $\text{BaTiO}_3\text{--}\text{MgFe}_2\text{O}_4$  composites have only rarely been investigated [14,15,16,17]. Tan et al. [14] synthesized  $\text{BaTiO}_3\text{--}\text{MgFe}_2\text{O}_4$  composites by a classical mixed-oxide method and found

an ME coefficient of  $50 \text{ mV cm}^{-1} \text{ Oe}^{-1}$ , while a two-step hybrid chemical process was examined by Tadi et al. [16].

The aim of this paper is to describe a fast and easy one-pot preparation route to obtain fine-grained  $\text{BaTiO}_3\text{--MgFe}_2\text{O}_4$  composite powders and ceramics with a 0–3 connectivity. The phase formation during the decomposition process was monitored by XRD and thermal analysis. The sintering behaviour and microstructure of resulting compacts were determined by dilatometry, SEM, and TEM. Magnetic measurements were carried out both on composite powders and ceramic bodies. For the latter, additional dielectric measurement are reported.

## 2. Experimental

### 2.1. Material preparation

Composites of  $(\text{BaTiO}_3)_{1-x}\text{--}(\text{MgFe}_2\text{O}_4)_x$  ( $x$  = weight fraction) were prepared using a modified Pechini-like process as described elsewhere [18]. The samples are abbreviated as BM– $x$  in the following.

For each composition freshly distilled  $\text{Ti}(\text{O}^i\text{C}_3\text{H}_7)_4$  (0.012 mol, Aldrich),  $\text{BaCO}_3$  (0.012 mol, Merck 1713, extra pure) and anhydrous citric acid (0.127 mol) were dissolved in 40 g 1,2-ethanediol at  $120^\circ\text{C}$  leading to a clear solution. Stoichiometric proportions of  $\text{Mg}(\text{NO}_3)_3\cdot 6\text{H}_2\text{O}$  (Alfa Aesar) and  $\text{Fe}(\text{NO}_3)_3\cdot 9\text{H}_2\text{O}$  (Merck) were separately dissolved in 20 g 1,2-ethanediol and added to the Ba/Ti-solution. The resulting final mixtures were continuously stirred at about  $180\text{--}190^\circ\text{C}$  until they turned to black-brown viscous gels. These gels were calcined for 1 h in static air at various temperatures from  $300^\circ\text{C}$  to  $1200^\circ\text{C}$  (heating-/cooling rate  $5 \text{ K min}^{-1}$ ).

To obtain ceramic bodies, BM– $x$  powders calcined at  $700^\circ\text{C}$  for 1 h, were uniaxially pressed into pellets (green density  $2.0 \text{ g cm}^{-3}$ ) without any pressing aid. The pellets were placed on a

ZrO<sub>2</sub> fibre mat and sintered to ceramic bodies up to 1250 °C with a rate of 10 K min<sup>-1</sup> and a soaking time of 1 h.

## **2.2. Characterization**

X-ray powder diffraction patterns were collected at room temperature on a *Bruker D8-Advanced* diffractometer, equipped with a one-dimensional silicon strip detector (LynxEye™) and operating with Cu-K<sub>α</sub> radiation. Dilatometric investigations were performed in flowing synthetic air (50 ml min<sup>-1</sup>) in a *Setaram TMA 92-16.18* dilatometer. Simultaneous thermogravimetric (TG) and differential thermoanalytic (DTA) measurements in flowing synthetic air (20 ml min<sup>-1</sup>) were performed using a *Netzsch STA 449* system. The TG/DTA measurements of the decomposition of the gel were carried out on a sample preheated at 250 °C for 30 min. TEM images were recorded with a *Philips CM20Twin* at an electron energy of 200 keV. Scanning electron microscope images were recorded with a *Philips XL30 ESEM* in the backscattered electron mode (BSE). Magnetic measurements were carried out using a *Quantum Design PPMS 9*. Hysteresis loops were taken at 300 K and 10 K with magnetic field cycling between -90 and +90 kOe. An Impedance Analyzer 4192A (Hewlett Packard) was used for permittivity measurements at room temperatures up to 13 MHz. As electrodes eutectic Ga-In alloy was coated on both sides of the ceramic bodies.

## **3. Results and discussion**

### **3.1. Powder characterization, TG-DTA, XRD**

Simultaneous TG/DTA investigations in flowing air (heating rate 5 K min<sup>-1</sup>) were carried out on a BM-0.3 gel preheated at 250 °C in air for 30 min (Fig. 1). A first weight loss of 44.1 % between 150 °C and 380 °C is accompanied by a weak exothermic signal with an onset temperature of 227 °C. A subsequent second step up to 510 °C causes a total weight loss of

82.5 % and is connected with two strong exothermic processes between 382 and 491 °C. Further heating to 1000 °C does not lead to any further significant weight loss. XRD measurements of the brown reaction product reveal the formation of  $\text{MgFe}_2\text{O}_4$  and  $\text{BaTiO}_3$  [19] without any impurity phases.

The phase evolution during the thermal decomposition up to 1200 °C of the black-brown homogenous gel was examined for BM-x samples with  $x = 0.1, 0.2, 0.3$ , and  $0.5$ . These gels were heated in a muffle furnace in static air at various temperatures for 1 h (rate  $5 \text{ K min}^{-1}$ ). As an example, in Fig. 2 the phase evolution for BM-0.3 is demonstrated. The starting BM-x-gel is completely X-ray amorphous (not shown). The XRD pattern of a sample calcined at 500 °C, i.e. above the final decomposition step, indicates the X-ray amorphous nature of the resulting orange-brown powder (Graph 2a). Only a weak and broad reflection at  $2\theta = 27^\circ$  suggests the formation of a barium oxycarbonate phase [20,21] which appears usually as an intermediate phase during the decomposition of (BaTi)-precursors [18]. After heat treatment at 600 °C (Graph 2b) reflections of  $\text{BaTiO}_3$ ,  $\text{MgFe}_2\text{O}_4$ ,  $\text{BaCO}_3$  [19], and traces of barium oxycarbonate can be observed. At 700 °C the carbonate phases vanish and only reflections of  $\text{BaTiO}_3$  and  $\text{MgFe}_2\text{O}_4$  are found (Graph 2c). Up to a calcination temperature of 1100 °C (Graph 2d) the powder samples consist of  $\text{BaTiO}_3$  and  $\text{MgFe}_2\text{O}_4$ . After calcination at 1200 °C very small traces of  $\text{BaFe}_{12}\text{O}_{19}$  appear. Only in the case of sample BM-0.5 (Graph 3a,b) we observe the partial formation (ca. 11 mol%) of hexagonal  $\text{BaTiO}_3$  [19] at 1200 °C. The colours of the calcination products (light-brown to brown) depend on the amount of  $\text{MgFe}_2\text{O}_4$ . Additionally, with increasing calcination temperature the colour gradually turns to dark-brown.

For powder BM-0.3 calcined at 700 °C for 1 h the volume-weighted average crystallite sizes for both  $\text{MgFe}_2\text{O}_4$  and  $\text{BaTiO}_3$  were calculated as 10 nm. Calcination at 800 °C results in crystallite sizes of 13 nm for  $\text{MgFe}_2\text{O}_4$  and 15 nm for  $\text{BaTiO}_3$  which increase to 31 and 41 nm

at 900 °C, respectively. TEM investigations on powder BM-0.3 calcined at 800 °C show particles mainly in the range of 18 to 30 nm (Fig. 4), which is in fairly good agreement with the XRD results.

### ***3.2. Sintering behaviour and microstructure***

Fig. 5 shows the non-isothermal dilatometric measurement up to 1300 °C in flowing air of compacts from powder BM-0.3 calcined at 700 °C for 1 h. The evolution of the relative densities was calculated assuming an isotropic shrinkage behaviour. A first weak shrinkage process starts at about 750 °C and above 1040 °C the shrinkage increases considerably. The shrinkage rate achieves a maximum at 1085 °C with a value of  $-0.80 \text{ \% min}^{-1}$ , which indicates sliding processes as the dominant shrinkage mechanism [22,23]. A final shrinkage process starts at 1230 °C and is not completed at the highest investigated temperature of 1300 °C.

The final bulk densities of ceramic bodies after isothermal conventional sintering (heating up with  $10 \text{ K min}^{-1}$ , soaking for 1 h, and cooling down with  $10 \text{ K min}^{-1}$ ) at various temperatures in static air are shown in Fig. 6. The absolute bulk densities of the sintered bodies were determined from their weight and geometric dimensions and the relative bulk densities were calculated with respect to the theoretical densities of 5.82 (BM-0.1), 5.64 (BM-0.2), 5.39 (BM-0.3), and  $5.26 \text{ g cm}^{-3}$  (BM-0.5) [24]. The absolute bulk densities decrease with increasing  $\text{MgFe}_2\text{O}_4$  content, primarily due to the lower crystallographic density of  $\text{MgFe}_2\text{O}_4$  ( $4.49 \text{ g cm}^{-3}$ ) compared to  $\text{BaTiO}_3$  ( $6.02 \text{ g cm}^{-3}$ ) [25,26]. Up to 1250 °C densities of 3.75 to  $4.72 \text{ g cm}^{-3}$  (rel. densities: 71–81 %) were reached. To improve the densification at temperatures below 1200 °C sintering additives would be necessary [27,28], which is the subject of a forthcoming paper.

Microstructures of selected sintered bodies are shown in Fig. 7. SEM images were recorded in the BSE mode. EDX measurements confirm that the white grains are  $\text{BaTiO}_3$  while the dark

particles are  $\text{MgFe}_2\text{O}_4$ . The light grey particles in Fig. 7c are mainly  $\text{BaTiO}_3$  particles tilted against the detector. The regular particle shapes (Fig. 7a,b) indicate a high crystallinity, i.e. the formation of submicron single crystals. Sintering at 1150 °C results in grain sizes between about 200 and 800 nm for BM-x ceramics with  $x = 0.1\text{--}0.5$ , while a lower sintering temperature of 1000 °C leads to grain sizes around 100–150 nm. The SEM images reveal the 0–3 connectivity of the composite ceramics. The grain sizes seem slightly to decrease with rising  $\text{MgFe}_2\text{O}_4$  content. On the other hand, the ferrite particles tend to be more irregularly shaped and to show increasing agglomeration with rising  $\text{MgFe}_2\text{O}_4$  content (Fig. 7c).

XRD patterns of ceramic bodies are shown in Fig. 8-10. After sintering at 1000 °C the ceramics consist of  $\text{BaTiO}_3$  and  $\text{MgFe}_2\text{O}_4$ , only. For  $T > 1100$  °C all ceramics contain barely detectable traces of  $\text{BaFe}_{12}\text{O}_{19}$  (Fig. 8). After sintering at 1200 °C the ceramic bodies of BM-0.3 and BM-0.5 show additional reflections of hexagonal  $\text{BaTiO}_3$  (Fig. 9). About 7 mol% (BM-0.3) and 65 mol% (BM-0.5) of  $\text{BaTiO}_3$  are converted to the hexagonal modification. After rising the sintering temperature to 1250 °C (Fig. 10) all ceramic samples show the appearance of hexagonal  $\text{BaTiO}_3$  with fractions of 3 mol% (BM-0.1), 56 mol% (BM-0.2), and 81 mol% (BM-0.3), respectively. In the case of BM-0.5  $\text{BaTiO}_3$  is even completely transformed to the hexagonal phase. The appearance of hexagonal  $\text{BaTiO}_3$  is the result of an increasing incorporation of  $\text{Fe}^{3+}$  into the  $\text{BaTiO}_3$  lattice [29,30] caused by larger contact areas between the particles due to the compaction.

### ***3.3. Magnetic and dielectric behaviour***

The dependence of magnetization (M) on the applied magnetic field (H) at 300 K for BM-0.3 powders calcined between 700 and 1200 °C for 1 h is depicted in Fig. 11. The other BM-x powders up to  $x = 0.5$  show an analogue behaviour. Up to 900 °C the saturation magnetization

increases with rising calcination temperature and thus increasing crystallite size. Calcining at 1200 °C leads to a gradually reduced saturation magnetization possibly due to reaction between BaTiO<sub>3</sub> and MgFe<sub>2</sub>O<sub>4</sub>. Changes in the inversion parameter of MgFe<sub>2</sub>O<sub>4</sub> phase is also a possible explanation [31,32]. The coercivity values ( $H_c$ ) at 300 K of BM-0.3 powders calcined between 700 and 900 °C are close to zero pointing to a superparamagnetic state of the magnesium ferrite particles. Temperature-dependent magnetization measurements (Fig. 12) show that the field-cooled (FC) curve increases with decreasing temperature, while the zero-field-cooled (ZFC) curve has a maximum at the so-called blocking temperature ( $T_B$ ), which reflects the transition between the superparamagnetic state (above  $T_B$ ) and the ferrimagnetic state (below  $T_B$ ) [33,34]. The blocking temperature increases with rising calcination temperature and in turn increasing particle size as seen in the inset of Fig. 12. Field-dependent magnetic measurement at 10 K (below  $T_B$ ) shows the formation of a pronounced hysteresis loop indicating the ferrimagnetic state as demonstrated in the inset in Fig. 11. Heating of BM- $x$  gels ( $x = 0.1, 0.2, 0.3, 0.5$ ) at 1000 °C and higher results in coercivities of 41–72 Oe at 300 K. These values are similar to the ones of pure MgFe<sub>2</sub>O<sub>4</sub> [35]. Fig. 13a shows the saturation magnetizations ( $M_s$ ) of BM- $x$  powders ( $x = 0.1$  to 1) calcined at 1000 °C for 1 h and selected BM- $x$  ceramic bodies (sintered at 1000 °C/ 1 h) as a function of the magnesium ferrite content ( $x$ ). The BM- $x$  powders and ceramic bodies show an almost identical behaviour. The saturation magnetization ( $M_s$ ) was evaluated by extrapolation of the high-field magnetization to  $H^{-1} \rightarrow 0$  according to the *Law of Approach to Saturation* [36]. The straight lines in Fig. 13a represent the expected calculated values based on the  $M_s$  value of pure magnesium ferrite (BM-1). These expected values are just approximations assuming that the particle size and the inversion parameter of MgFe<sub>2</sub>O<sub>4</sub> do not change. The  $M_s$  values (related to the sample mass) at 300 K differ only slightly from the expected values. In contrast the  $M_s$  values measured at 10 K are significantly higher than the expected ones. Additionally,



as seen in the inset of Fig. 13a, the  $M_s$  values (related to the  $\text{MgFe}_2\text{O}_4$  mass) show a strong increase with decreasing  $\text{MgFe}_2\text{O}_4$  content. The measurements at 10 K reveal a paramagnetic contribution in addition to the ferrimagnetic moment. As a consequence the  $M_s$  values estimated by the  $H^{-1} \rightarrow 0$  method are too high by trend. This paramagnetic moment is not clearly observed at 300 K because of its  $T^{-1}$  dependence. Fig. 14 exemplarily shows the hysteresis loops at 10 K of BM-0.2, BM-0.5 and BM-1 calcined at 1000 °C for 1 h indicating an increasing paramagnetic contribution with decreasing magnesium ferrite fraction. This finding can be explained assuming that diffusion of  $\text{Fe}^{3+}$  from the  $\text{MgFe}_2\text{O}_4$  to the  $\text{BaTiO}_3$  phase at the grain boundaries results in paramagnetic centres [29,37,38,39,40]. A decreasing fraction of  $\text{MgFe}_2\text{O}_4$  leads to an enhanced embedding of the ferrite phase between the  $\text{BaTiO}_3$  particles resulting in larger contact areas. As seen in the SEM images (Fig. 7) an increasing  $\text{MgFe}_2\text{O}_4$  content results in a higher agglomeration rate of the ferrite particles and a decreasing homogenous distribution of  $\text{MgFe}_2\text{O}_4$  and  $\text{BaTiO}_3$ . The assumption of a possible reaction between  $\text{BaTiO}_3$  and  $\text{MgFe}_2\text{O}_4$  is supported by the appearance of hexagonal  $\text{BaTiO}_3$  after heat treatment at 1200–1250 °C (see Fig. 3,9,10). In pure  $\text{BaTiO}_3$  the hexagonal modification is formed at about 1460 °C [41,42], whereas the temperature for the formation of hexagonal  $\text{BaTiO}_3$  can be significantly reduced by incorporating of iron into the  $\text{BaTiO}_3$  lattice [29,30,43].

To estimate the saturation magnetization at 10 K originating from the ferrimagnetic  $\text{MgFe}_2\text{O}_4$  phase,  $M_s$  was calculated by a linear extrapolation to  $H = 0$  of the magnetization at high fields versus  $H$ , assuming that the increase in magnetization at high field is dominated by the paramagnetic contribution according to *Speliotis* and *Fernelius* [44]. Using this method, the  $M_s$  values at 10 K are very close to the expected ones (Fig. 13b). The observed  $M_s$  values (related to the sample mass) at 300 K are slightly lower than the expected ones. This behaviour is most likely caused by a surface effect due to the formation of grain boundaries between  $\text{BaTiO}_3$  and  $\text{MgFe}_2\text{O}_4$  and was also observed in  $\text{CoFe}_2\text{O}_4$ – $\text{BaTiO}_3$  composites

[45,46]. The grain boundaries of the ferrite particles are characterized by a reduced magnetic ordering [45,47]. On the other hand cation redistribution between  $\text{Mg}^{2+}$  and  $\text{Fe}^{3+}$ , which influences the magnetization values, cannot be ruled out either.

Therefore, the saturation magnetization of composites with low ferrite content should be calculated by extrapolation of the magnetization to  $H = 0$  instead to  $H^{-1} \rightarrow 0$ , especially at low temperatures, in contrast to pure ferrite samples.

Fig. 15 shows the M–H loops at 300 K of ceramic bodies sintered at 1150 °C. The increase of the ferrite content corresponds to rising magnetization values, which are larger than the ones reported for  $\text{MgFe}_2\text{O}_4$ – $\text{BaTiO}_3$  composites obtained by a classical mixed-oxides process [14]. All ceramic samples reveal that the  $M_s$  and  $H_c$  values reach a maximum at sintering temperatures between 1100–1150 °C. The coercivities are rather small with a maximum value of 63 Oe.

Fig. 16 shows the variation of the relative permittivity ( $\epsilon_r$ ) and dissipation factor ( $\tan \delta$ ) depending on the applied frequency for ceramic bodies of  $\text{BaTiO}_3$  (BM–0),  $\text{MgFe}_2\text{O}_4$  (BM–1), and composites (BM–x). All samples exhibit slightly decreasing permittivities and loss tangent values with increasing frequency. Between about 0.5 MHz and 13 MHz the relative permittivities of the composite samples change only slightly. An increasing  $\text{MgFe}_2\text{O}_4$  fraction (x) leads to lower permittivities. On the other hand, the dissipation factor ( $\tan \delta$ ) increases with rising  $\text{MgFe}_2\text{O}_4$  content, because of the electrically leaky nature of ferrites (Fig. 16b). The relative permittivities of BM–0.3 ceramic bodies depending on the sintering temperatures are demonstrated in Fig. 17. Increasing sintering temperatures result in raising permittivity values predominantly due to the increasing densities of the bodies. However, after sintering at 1250 °C the permittivity decreases because of the formation of large quantities of hexagonal  $\text{BaTiO}_3$  [48,49] (see Fig. 10). The inset in Fig. 17 shows the relative permittivities of BM–0.1 and BM–0.2 ceramics sintered at 1200 °C. For composite samples

with an  $\text{MgFe}_2\text{O}_4$  content lower than 50 wt.% the relative permittivity values are higher and the dissipation factor is lower than for  $\text{BaTiO}_3$ – $\text{MgFe}_2\text{O}_4$  composites prepared by a two-step hybrid process [16].

## Conclusion

$(\text{BaTiO}_3)_{1-x} - (\text{MgFe}_2\text{O}_4)_x$  composite samples (BM–x) were synthesized by a one-pot process using 1,2-ethandiol and citric acid to form a gel in which the components are distributed on an atomic level. Composite samples up to  $x = 0.5$  (weight fraction) were investigated in detail. Calcination of homogeneous viscous BM–x gels at  $T \geq 700\text{ }^\circ\text{C}$  leads to composite powders consisting of  $\text{BaTiO}_3$  and  $\text{MgFe}_2\text{O}_4$ . The nano-scaled ferrite particles show a superparamagnetic behaviour. Non-isothermal dilatometric measurements show that a weak shrinkage process starts at about  $750\text{ }^\circ\text{C}$  and a significant shrinkage occurs above  $1040\text{ }^\circ\text{C}$ . Ceramic bodies were obtained after isothermal sintering for 1 h between  $1000$  and  $1250\text{ }^\circ\text{C}$  and reached relative densities up to 81 %. SEM images show that the  $\text{MgFe}_2\text{O}_4$  particles are surrounded by  $\text{BaTiO}_3$  with a 0–3 connectivity. Magnetic measurements on powders and ceramic bodies treated at  $1000\text{ }^\circ\text{C}$  and higher show ferrimagnetic behaviour with coercivity values up to 63 Oe at 300 K. Measurements at 10 K reveal the presence of a small paramagnetic contribution in addition to the ferrimagnetic behaviour. In particular for composites with low  $\text{MgFe}_2\text{O}_4$  content the magnetic saturation is not yet reached at 90 kOe, suggesting that the hysteresis loop is overlayed by a paramagnetic contribution. The relative permittivities of the BM–x ceramics decrease with increasing ferrite content, while their dissipation factors increase. Additionally, rising sintering temperature up to  $1200\text{ }^\circ\text{C}$  leads to larger permittivities.

The resulting fine-grained composite ceramics are potential candidates for ME applications. Investigations of the magneto-electrical effect are in progress.

## **Acknowledgements**

Financial support by the German Science Foundation within the Collaborative Research Centre (SFB 762) *Functionality of Oxide Interfaces* (INST271/240-2) is gratefully acknowledged.

## **Captions**

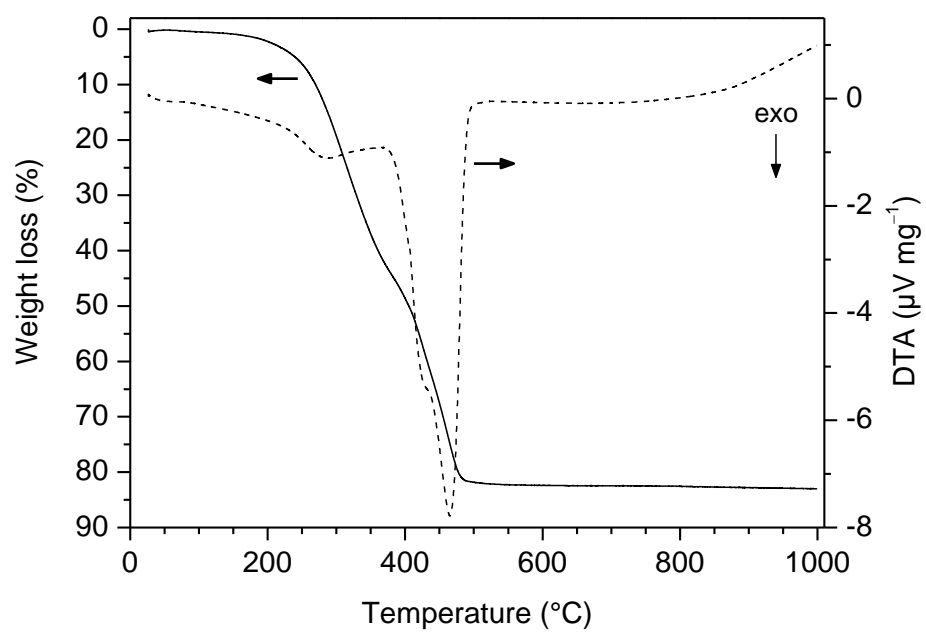


**Fig. 1**

Simultaneous TG/DTA investigation of a preheated BM-0.3 gel in flowing air (heating rate of  $5 \text{ K min}^{-1}$ ).

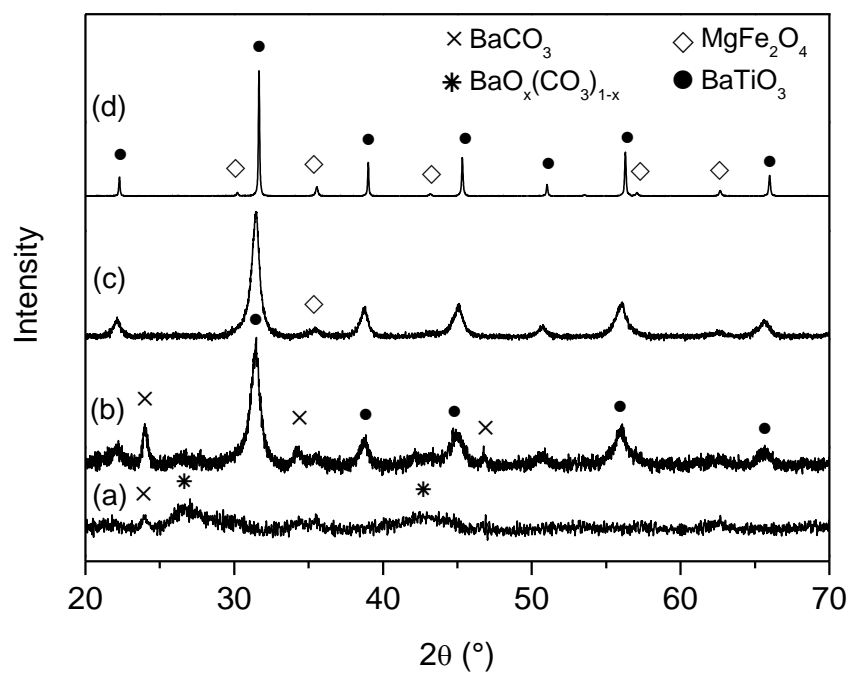


**Fig. 2**

Room temperature XRD patterns after calcination of the BM-0.3 gel at various temperatures (rate: 5 K min<sup>-1</sup>): (a) 500 °C, 1 h; (b) 600 °C, 1 h; (c) 700 °C, 1 h; (d) 1100 °C, 1 h.

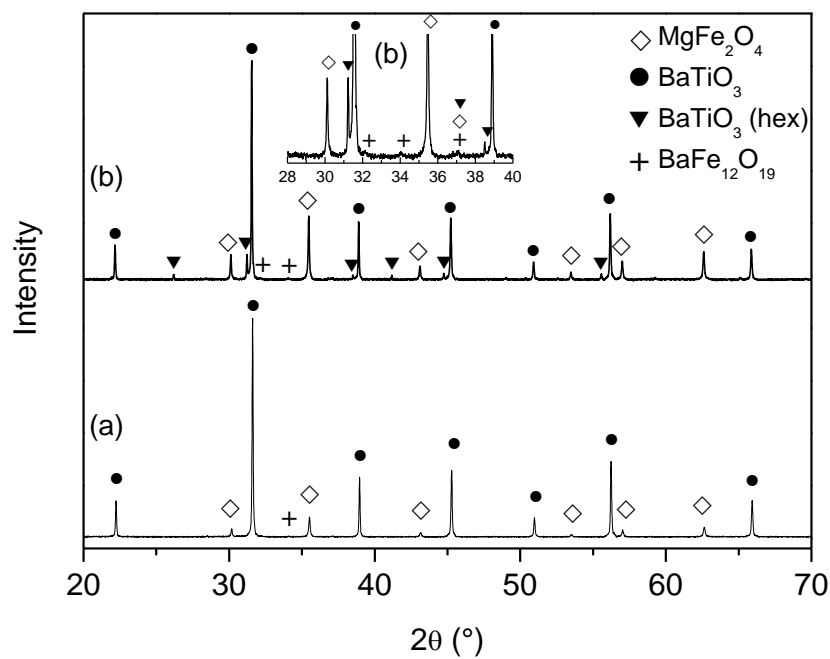


**Fig. 3**

Room temperature XRD patterns after calcination at 1200 °C for 1 h (rate: 5 K min<sup>-1</sup>) of (a) BM-0.3 and (b) BM-0.5.

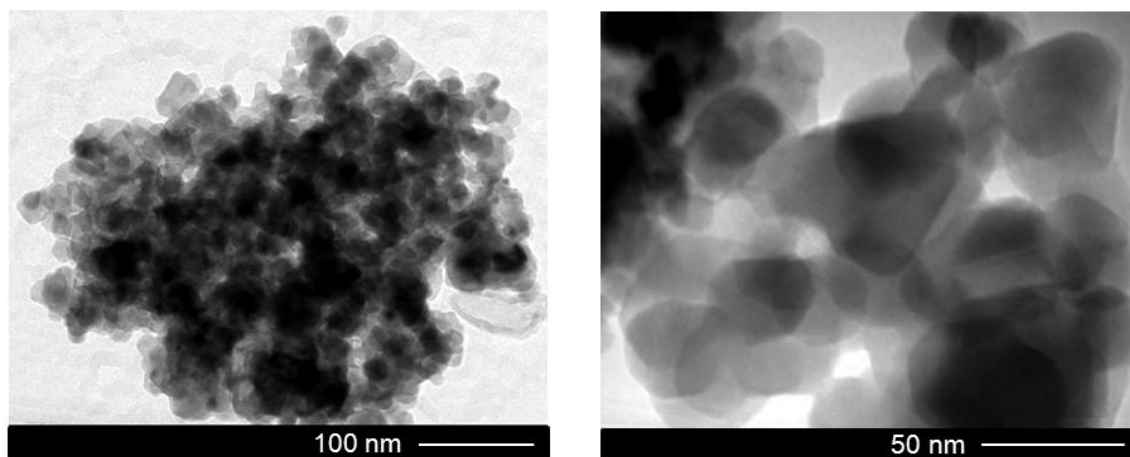


**Fig. 4**

TEM images of BM-0.3 powder calcined at 800 °C for 1 h.

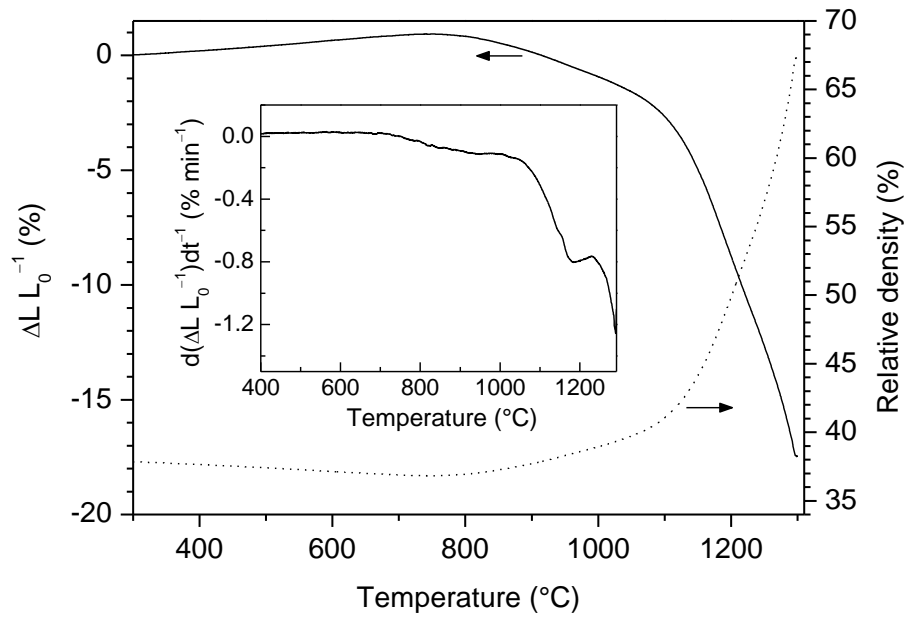


**Fig. 5**

Non-isothermal dilatometric measurements in flowing air of compacts of BM-0.3 (calcined at 700 °C) with a heating rate of 10 K min<sup>-1</sup>. The inset shows the relative shrinkage rates ( $d(\Delta L/L_0)/dt$ ).



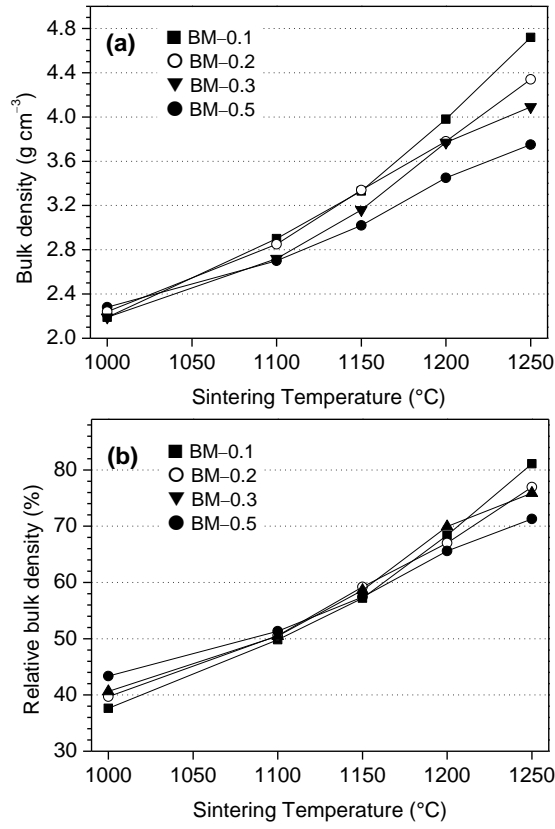


**Fig. 6**

Final bulk densities versus sintering temperature (soaking time 1 h, rate 10 K min<sup>-1</sup>) of ceramic bodies from BM-x powders calcined at 700 °C. (a) absolute bulk densities, (b) relative bulk densities.

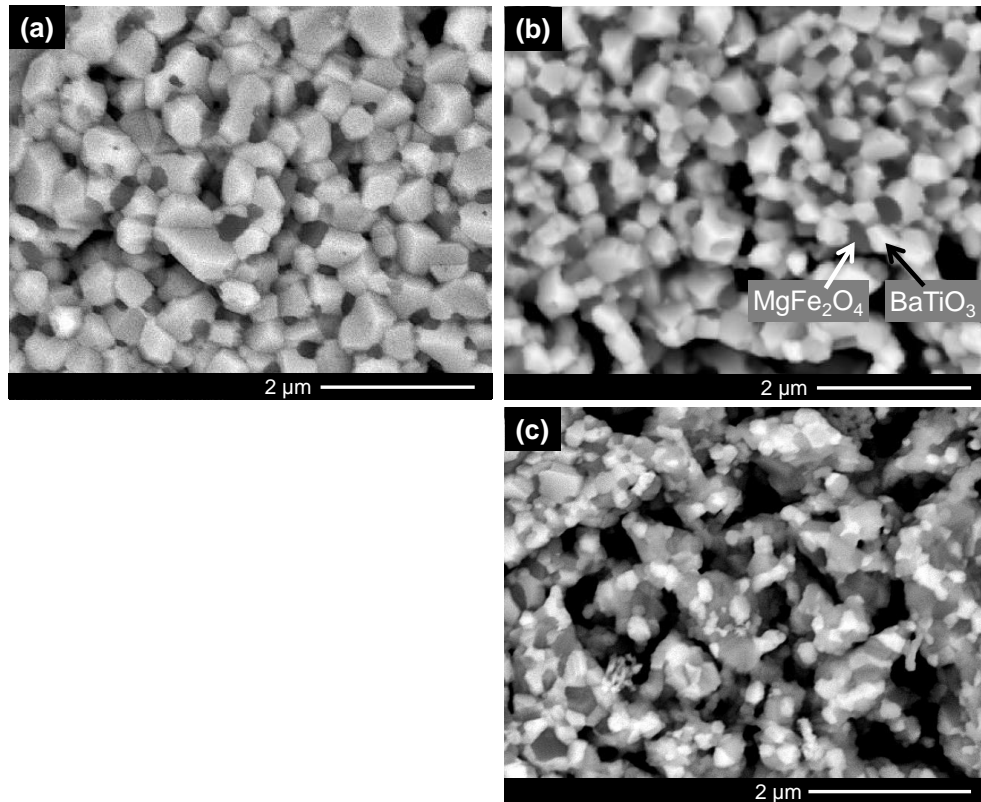


**Fig. 7**

SEM-BSE images of ceramic bodies sintered at 1150 °C for 1 h. (a) BM-0.1 (b) BM-0.2, (c) BM-0.5.

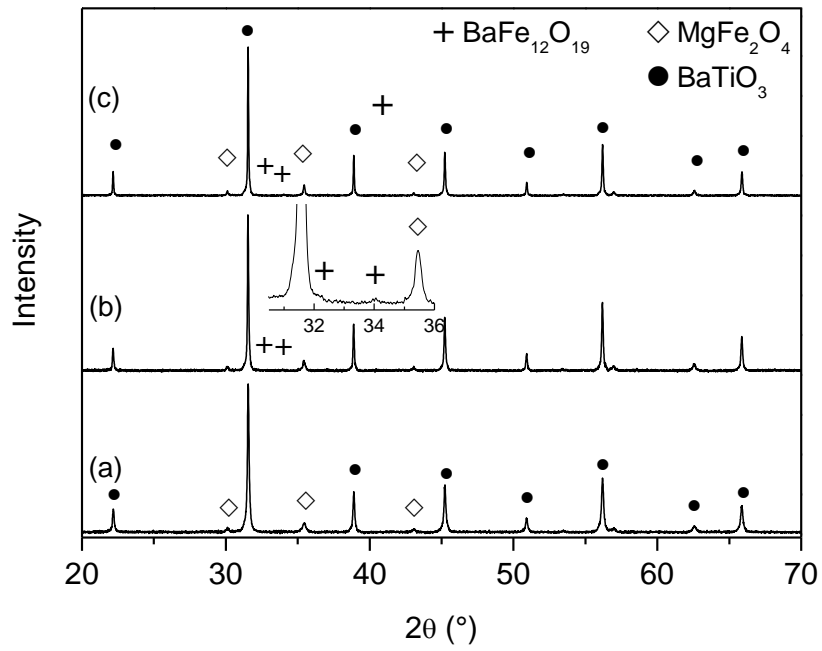


**Fig. 8**

Room temperature XRD patterns of BM-0.3 ceramic bodies after sintering for 1 h. (a) 1000 °C (b) 1100 °C, (c) 1150 °C.

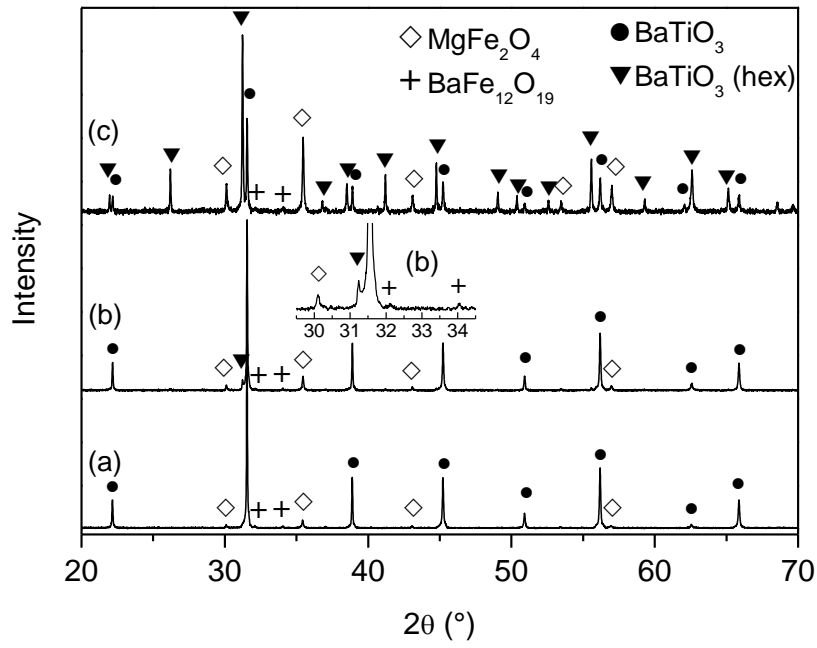


**Fig. 9**

Room temperature XRD patterns of ceramic bodies after sintering at 1200 °C for 1 h. (a) BM-0.2, (b) BM-0.3, and (c) BM-0.5.

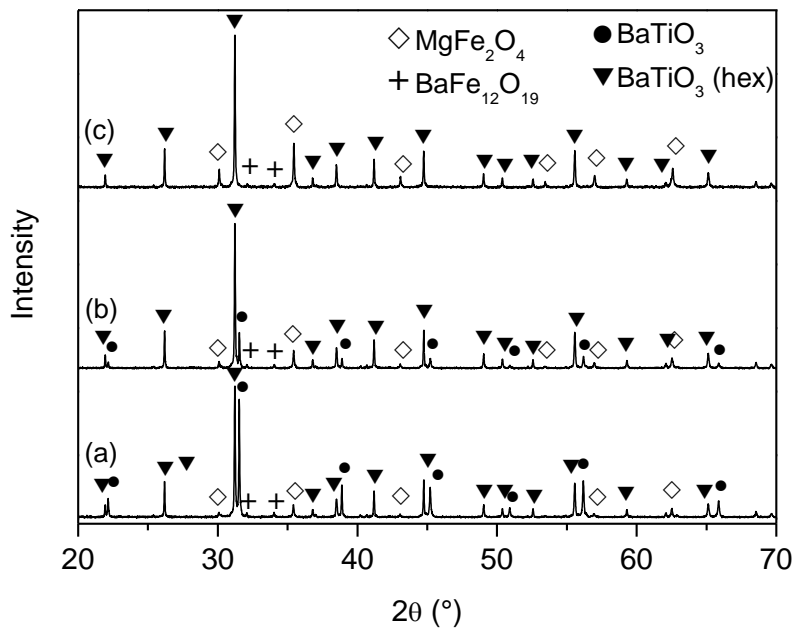


**Fig. 10**

Room temperature XRD patterns of ceramic bodies after sintering at 1250 °C for 1 h. (a) BM-0.2, (b) BM-0.3, and (c) BM-0.5.

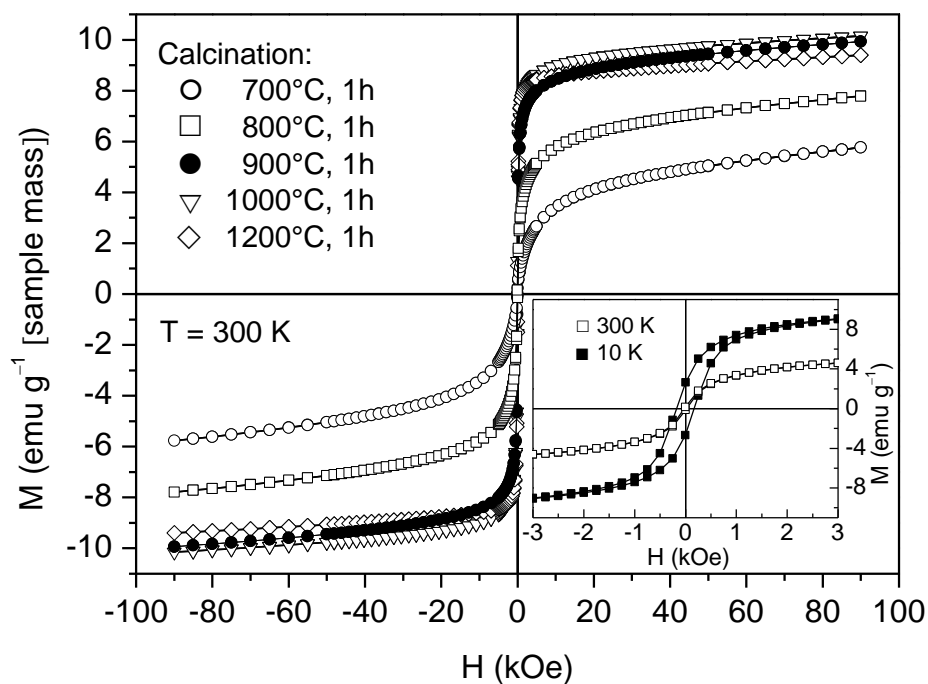


**Fig. 11**

Magnetization (M) versus applied magnetic field (H) at 300 K for BM-0.3 powders after calcining at different temperatures. The inset shows M versus H in the low-field range measured at 300 and 10 K for powder BM-0.3 calcined at 800 °C. The magnetization is related to the sample mass.

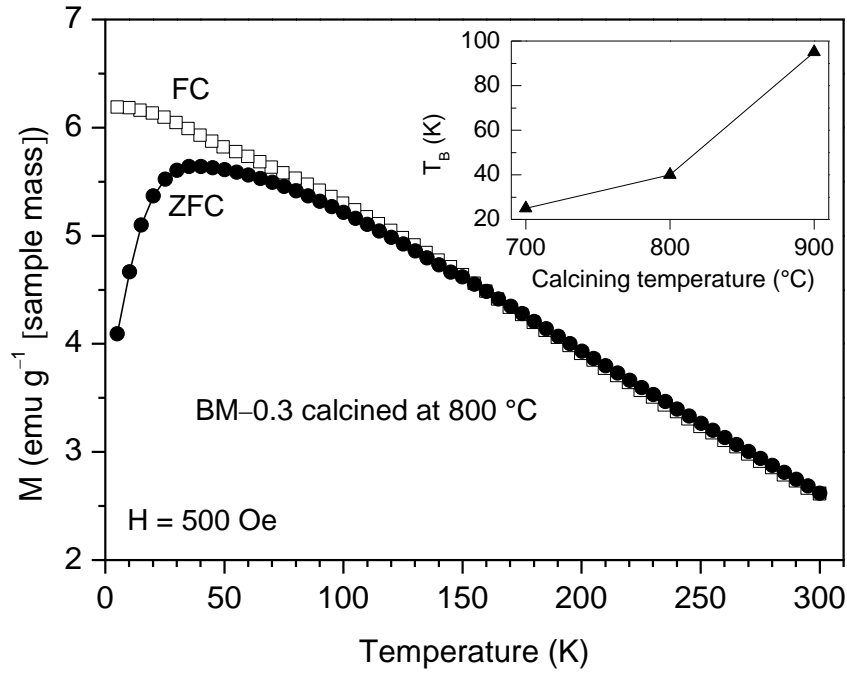


**Fig. 12**

Temperature dependence (5–300 K) of the magnetization under zero-field cooled (ZFC) and field-cooled (FC) conditions for powder BM-0.3 calcined at  $800^\circ\text{C}$ . The inset shows the dependence of the blocking temperature ( $T_B$ ) on the calcination temperature. The magnetization is related to the sample mass.

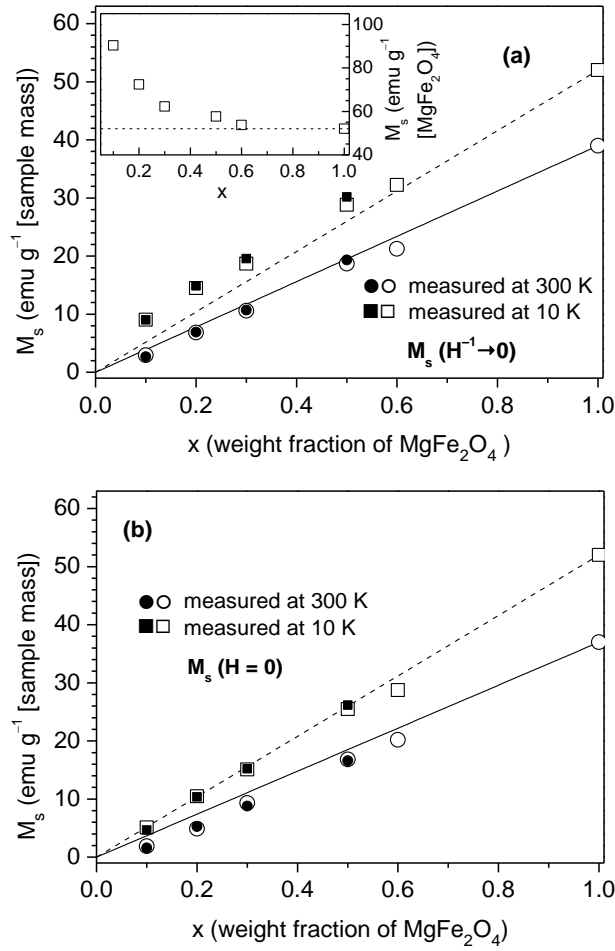


**Fig. 13**

Dependence of the saturation magnetization ( $M_s$ ), related to the whole sample mass, on the weight fraction of  $\text{MgFe}_2\text{O}_4$  ( $x$ ) of BM- $x$  powders ( $\circ, \square$ ) and ceramics ( $\bullet, \blacksquare$ ) calcined/-sintered at 1000 °C for 1 h. (a)  $M_s$  is estimated by the  $H^{-1} \rightarrow 0$  method. In the inset  $M_s$  is related only to the  $\text{MgFe}_2\text{O}_4$  mass. (b)  $M_s$  is estimated by the  $H = 0$  method.

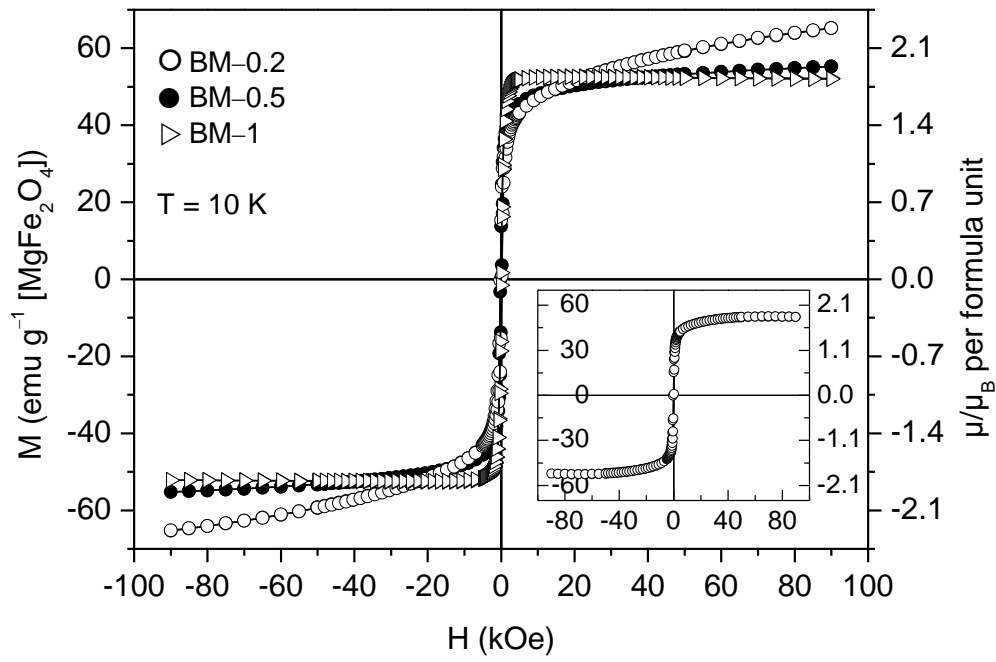


**Fig. 14**

Magnetization ( $M$ ) versus applied magnetic field ( $H$ ) at 10 K for selected BM- $x$  powders calcined at 1000 °C for 1 h. The inset shows  $M$  versus  $H$  after subtracting of the paramagnetic contribution for the BM-0.2 powder. The magnetization is given with respect to the  $\text{MgFe}_2\text{O}_4$  mass.



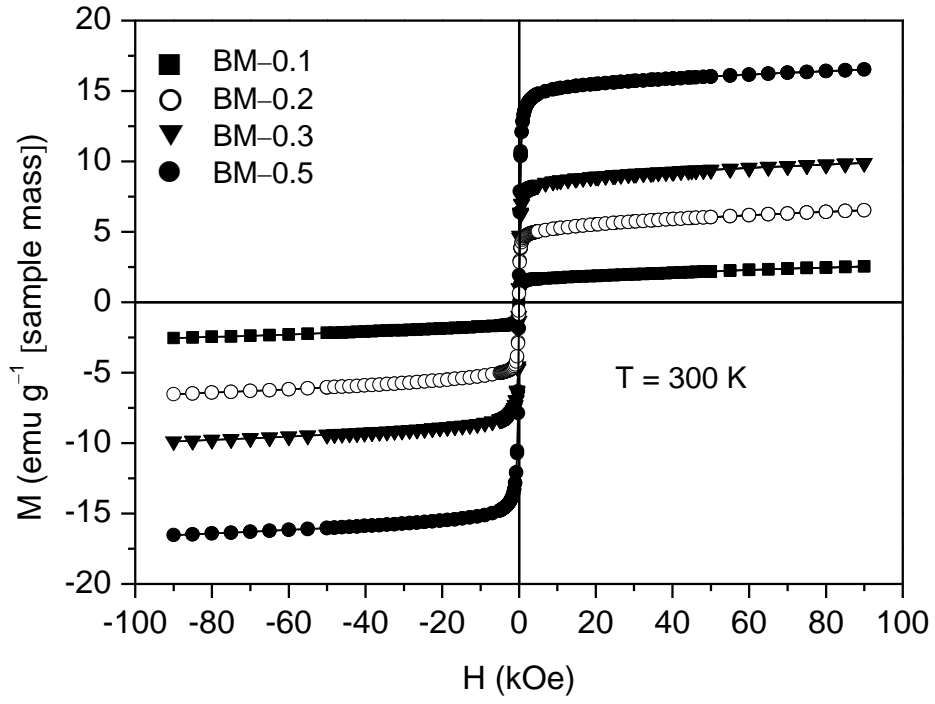


**Fig. 15**

Magnetization (M) versus applied magnetic field (H) at 300 K for BM-x ceramic bodies sintered at 1150 °C for 1 h. The magnetization is calculated with respect to the sample mass.

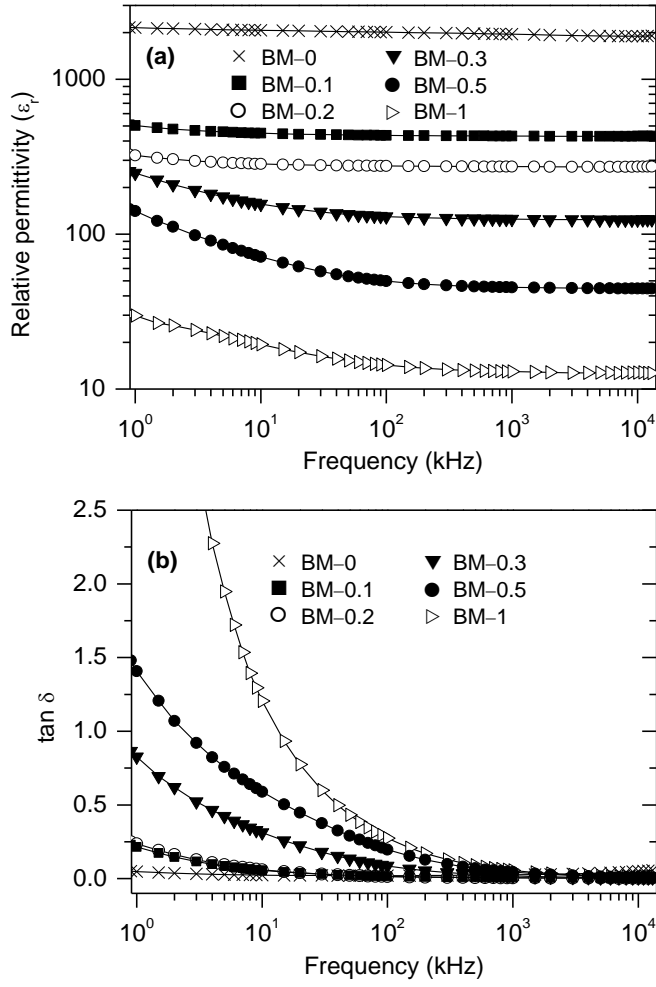


**Fig. 16**

Dependence of the real part of the relative permittivity ( $\epsilon_r$ ) (a) and the dissipation factor ( $\tan \delta$ ) (b) on the frequency at room temperature for BM-x ceramic bodies sintered at 1150 °C for 1 h.

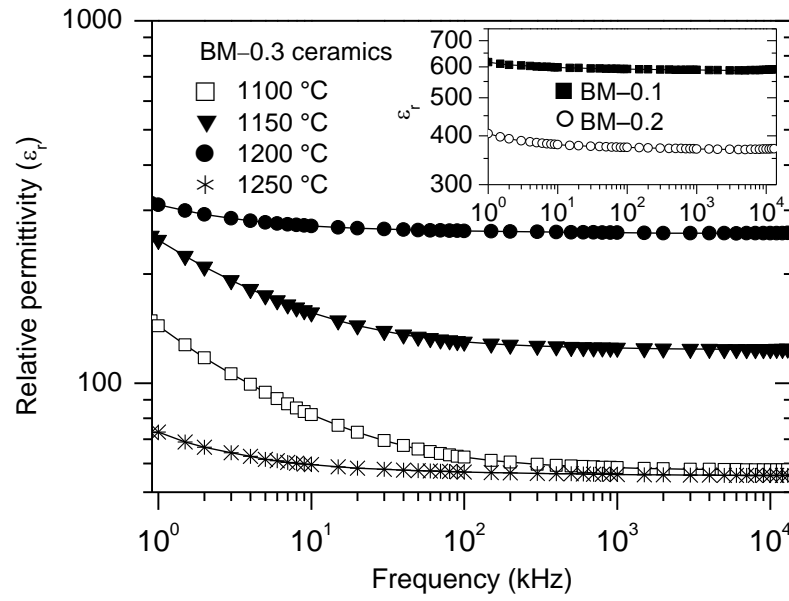


**Fig. 17**

Dependence of the real part of the relative permittivity ( $\epsilon_r$ ) on the frequency at room temperature for BM-0.3 ceramic bodies sintered at different temperatures for 1 h. The inset shows the relative permittivity for BM-0.1/0.2 ceramics sintered at 1200 °C.

## References

- [1] C.-W. Nan, M.I. Bichurin, S. Dong, D. Viehland, G. Srinivasan, J. Appl. Phys. 103 (2008) 031101.
- [2] J. Ma, J. Hu, Z. Li, C.-W. Nan, Adv. Mater. 23 (2011) 1062–1087.
- [3] J.F. Scott, Nat. Mater. 6 (2007) 256–257.

- 
- [4] J. Ryu, S. Priya, K. Uchino, H.-E. Kim, *J. Electroceram.* 8 (2002) 107–119
- [5] A. Gupta and R. Chatterjee, *J. Eur. Ceram. Soc.* 33 (2013) 1017–1022.
- [6] R.P. Mahajan, K.K. Patankar, M.B. Kothale, S.A. Patil, *Bull. Mater. Sci.* 23 (2000) 273–279.
- [7] S.Q. Ren, L.Q. Weng, S.-H. Song, F. Li, *J. Mater. Sci.* 40 (2005) 4375–4378.
- [8] R.S. Devan and B.K. Chougule, *J. Appl. Phys.* 101 (2007) 014109.
- [9] P. Zhu, Q. Zheng, R. Sun, W. Zhang, J. Gao, C. Wong, *J. Alloys Compd.* 614 (2014) 289–296.
- [10] Y. Liu, Y. Wu, D. Li, Y. Zhang, J. Zhang, J. Yang, *J. Mater. Sci.: Mater. Electron.* 24 (2014) 1900–1904.
- [11] R. Liu, Y. Thao, R. Huang, Y. Zhao, H. Zhou, *J. Mater. Chem.* 20 (2010) 10665–10670.
- [12] L.V. Leonel, J.B. Silva, A. S. Albuquerque, J.D. Ardisson, W.A.A. Macedo, N.D.S. Mohallem, *J. Phys. Chem. Solids* 73 (2012) 1362–1371.
- [13] J. van den Boomgaard and R.A.J. Born, *J. Mater. Sci.* 13 (1978) 1538–1548.
- [14] S.Y. Tan, S.R. Shannigrahi, S.H. Tan, F.E.H. Tay, *J. Appl. Phys.* 103 (2008) 094105.
- [15] R. Tadi, Y.-Il Kim, K.-S. Ryu, *J. Korean Phys. Soc.* 61 (2012) 1545–1549.
- [16] R. Tadi, Y.-Il Kim, D. Sarkar, C. Kim, K.-S. Ryu, *J. Magn. Magn. Mater.* 323 (2011) 564–568.
- [17] V.S. Bushkova and A.V. Kopayev, *Fizika i Khimiya Tverdogo Tila* 13 (2012) 363–368.
- [18] M. Arima, M. Kakihana, Y. Nakamura, M. Yashima, M. Yoshimura, *J. Am. Ceram. Soc.* 79 (1996) 2847–2856.
- [19] PDF 2 (International Centre for Diffraction Data, Pennsylvania) 2001, BaTiO<sub>3</sub> [81-2201]<sub>tetragonal</sub>, BaTiO<sub>3</sub> [82-1175]<sub>hexagonal</sub>, MgFe<sub>2</sub>O<sub>4</sub> [71-1232]<sub>cubic</sub>, BaFe<sub>12</sub>O<sub>19</sub> [84-757]<sub>hexagonal</sub>, BaCO<sub>3</sub> [5-378]<sub>orthorhombic</sub>.

- 
- [20] V. Ischenko, J. Woltersdorf, E. Pippel, R. Köferstein, H.-P. Abicht, *Solid State Sci.* 9 (2007) 303–309
- [21] V. Ischenko, E. Pippel, R. Köferstein, H.-P. Abicht, J. Woltersdorf, *Solid State Sci.* 9 (2007) 21–26
- [22] R. Köferstein, L. Jäger, M. Zenkner, S.G. Ebbinghaus, *J. Eur. Ceram. Soc.* 29 (2009) 2317–2324.
- [23] W. Schatt, *Sintervorgänge*, VDI-Verlag, Düsseldorf, 1992.
- [24] M. Zenkner, L. Jäger, R. Köferstein, H.-P. Abicht, *Solid State Sci.* 10 (2008) 1556–1562.
- [25] M. Pailhe, A. Wattiaux, M. Gaudon, A. Demourgues, *J. Solid State Chem.* 181 (2008) 1040–1047
- [26] G.H. Kwei, A.C. Lawson, S.J.L. Billinge, S.-W. Cheong, *J. Phys. Chem.* 97 (1993) 2368–2377.
- [27] R. Köferstein, L. Jäger, M. Zenkner, T. Müller, S.G. Ebbinghaus, *J. Eur. Ceram. Soc.* 30 (2010) 1419–1425
- [28] R. Köferstein, L. Jäger, M. Zenkner, H.-P. Abicht, *J. Mater. Sci.* 43 (2008) 832–838.
- [29] R. Böttcher, H.T. Langhammer, T. Müller, H.-P. Abicht, *J. Phys.: Condens. Matter* 20 (2008) 505209.
- [30] T.A. Vanderah, J.M. Loezos, R.S. Roth, *J. Solid State Chem.* 121 (1996) 38–50.
- [31] J. Chandradass, A.H. Jadhav, H. Kim, *Appl. Surf. Sci.* 258 (2012) 3315–3320.
- [32] C. J. Krissman, S. E. Harrison, *Phys. Rev.* 103 (1956) 857–860
- [33] L.D. Tung, V. Kolesnichenko, D. Caruntu, N.H. Chou, C.J. O'Connor, L. Spinu, *J. Appl. Phys.* 93 (2003) 7486–7488.
- [34] M. Sasaki, P.E. Jönsson, H. Takayama, H. Mamiya, *Phys. Rev. B* 71 (2005) 104405.

- 
- [35] R. Köferstein, T. Walther, D. Hesse, S.G. Ebbinghaus, *J. Mater. Sci.* 48 (2013) 6509–6518.
- [36] S. Chikazumi, *Physics of Ferromagnetism*, Oxford University Press, 2005.
- [37] S. Ray, P. Mahadevan, S. Mandal, S.R. Krishnakumar, C.S. Kuroda, T. Sasaki, T. Taniyama, M. Itoh, *Phys. Rev. B* 77 (2008) 104416.
- [38] X.K. Wei, Y.T. Su, Y. Sui, Q.H. Zhang, Y. Yao, C.Q. Jin, R.C. Yu, *J. Appl. Phys.* 110 (2011) 114112.
- [39] S. Qiu, W. Li, Y. Liu, G. Liu, Y. Wu, N. Chen, *Trans. Nonferrous Met. Soc. China* 20 (2010) 1911–1915.
- [40] A. Mishra and N. Mishra, *Int. J. Mater. Sci. Appl.* 1 (2012) 14–21.
- [41] S. Lee, C.A. Randall, Z.-K. Liu, *J. Am. Ceram. Soc.* 90 (2007) 2589–2594.
- [42] K.W. Kirby and B.A. Wechsler, *J. Am. Ceram. Soc.* 74 (1991) 1841–1847.
- [43] N. Maso, H. Beltran, E. Cordoncillo, P. Escribano, A.R. West, *J. Mater. Chem.* 16 (2006) 1626–1633.
- [44] D.E. Spiliotis and N.C. Fernelius, *J. Appl. Phys.* 61 (1987) 3831–3833.
- [45] J.P. Chen, C.M. Sorensen, K.J. Klabunde, G.C. Hadjipanayis, E. Devlin, A. Kostikas, *Phys. Rev.* 54 (1996) 9288–9296.
- [46] V. Corral-Flores, D. Bueno-Baques, R.F. Ziolo, *Acta Mater.* 58 (2010) 764–769.
- [47] S. Haffer, T. Walther, R. Köferstein, S.G. Ebbinghaus, M. Tiemann, *J. Phys. Chem. C* 117 (2013) 24471–24478.
- [48] Y. Akishige, G. Oomi, T. Yamamoto, E. Sawaguchi, *J. Phys. Soc. Jpn.* 58 (1989) 930–939.
- [49] J. Yu, P.-F. Paradis, T. Ishikawa, S. Yoda, *Jpn. J. Appl. Phys.* 43 (2004) 8135–8138.